PAPER

Physicochemical properties of the AC-excited helium discharges using a water electrode

Plasma Sci. Technol. **20** (2018) 075403 (9pp) https://doi.org/10.1088/2058-6272/aab4f2

Physicochemical properties of the AC-excited helium discharges using a water electrode

Hafiz Imran Ahmad QAZI[1], **Yiying XIN** (辛怡颖)[2], **Muhammad Ajmal KHAN**[1], **Heping LI** (李和平)[1,3], **Lu ZHOU** (周律)[2,3] **and Chengyu BAO** (包成玉)[1]

[1] Department of Engineering Physics, Tsinghua University, Beijing 100084, People's Republic of China
[2] School of Environment, Tsinghua University, Beijing 100084, People's Republic of China

E-mail: liheping@tsinghua.edu.cn and zhou2001@263.net.cn

Received 29 November 2017, revised 7 March 2018
Accepted for publication 7 March 2018
Published 29 May 2018

Abstract

In this paper, the AC-excited helium discharges generated between the powered needle electrode enclosed in a conical quartz tube and the grounded de-ionized water electrode are investigated. The current and voltage waveforms exhibit a transition from the glow-like to streamer-like mode discharges, which forms a stable cone-shaped structure at the gas–liquid interface. In this region, the air and water vapor diffusion initiate various physical–chemical processes leading to substantial changes of the primary species emission intensities (e.g., OH, N_2, NO, and O) and the rotational temperatures. The experimentally measured rotational temperature at the gas–liquid interface is 870 K from the N_2(C–B) band with a power input of 26 W. With the prolongation of the discharge time, significant changes in the discharge voltage and current, discharge emission patterns, instantaneous concentrations of the secondary species (e.g., H_2O_2, NO_2^-, and NO_3^-) in the liquid phase, pH values and electrical conductivities of the liquids are observed experimentally. The present study is helpful for deepening the understandings to the basic physical–chemical processes in the discharges in contact with liquids, especially to those occurring in the vicinity of the gas–liquid interface, and also for promoting existing and potential applications of such type of discharges in the fields of environmental protection, biomedicine, agriculture, and so on.

Keywords: solution plasma, gas–liquid interface, wastewater treatment, biomedical science and agriculture applications

(Some figures may appear in colour only in the online journal)

1. Introduction

Over the past decades, there have been increasing interests on the electrical discharges in contact with liquid, which is due to their potential applications in various fields, such as environmental protection, biomedical science, agriculture and nano-scale materials synthesis [1–4]. Deep understandings to the complex multi-phase discharges due to the involvement of water vapor are crucial for promoting their various actual applications [5–7]. The characteristics of the discharges in contact with liquid are dependent on various factors, such as compositions of the plasma forming gases, nature of the liquid, power input, driving frequency, and plasma treatment time. These factors influence the physical–chemical properties of the discharges including formation of primary species (e.g., OH, N_2, NO, and O) at the gas–liquid interface, electron and heavy-particle temperatures, and secondary species (e.g., H_2O_2, NO_2^-, and NO_3^-) concentrations into the liquid phase which ultimately affect the liquid properties. In particular, higher water vapor concentrations at the gas–liquid interface not only induce variations in the physical processes but also stimulate the plasma chemistry which initiates different

[3] Authors to whom any correspondence should be addressed.

chemical reactions with dissolving of the primary species into liquid. This is one of the reasons why the studies on the characteristics of the discharges in contact with liquids have attracted much attention of the researchers recently, especially focusing on the plasma features in the vicinity of the gas–liquid interface [2, 7–13].

From the aspect of applications, these chemically reactive species produced during discharges are demanding in various fields. For example, OH and H_2O_2 radicals are highly reactive [14–17] and responsible for the advanced oxidation processes [16] results in the removal of organic contamination from polluted water [16, 17]; NO diffusion through most of tissues makes it suitable for tissue/wound healing [18]; O is an effective agent for cell destructions and for liquid disinfections [19]; NO_2^- induces cell apoptosis through DNA damages and can be employed for cancer therapy [20, 21]; while NO_3^- is an important fertilizer for stimulating growth of plants [3, 22]. From the aspect of fundamental studies on the discharge itself, the complicated physical–chemical processes involving water vapor with high concentrations at the gas–liquid interface make the control of plasma key parameters and the formation mechanisms of primary species more challenging [7, 9, 23, 24]. In addition, the changes in the concentrations of secondary species in the liquid phase with increasing discharge time using various plasma forming gases are important due to their application diversity in numerous fields [2, 3]. And this also provides insights in understanding various chemical reactions into liquid initiated by plasmas in the gas–liquid environment. For the discharges in contact with liquid, the chemically reactive species upon dissolving into the liquid phase can change the liquid pH values and electrical conductivities, which affects the formation of secondary species by stimulating certain chemical processes in the liquid phase. This makes the plasma–liquid interaction be much more complicated. Recently, the secondary species concentrations were measured as a function of different gas compositions (e.g., 20% O_2 in N_2 or 20% O_2 in Ar) in a pulsed discharge with a 50 Hz repetition frequency and a high voltage pulse of 27 kV in a solution with constant pH values 3.3, 6.9 and 10.1. The experimental results showed that, with the prolongation of the discharge time, the concentrations of H_2O_2, NO_2^- and NO_3^- increased in the solutions with higher pH values. While the concentrations of H_2O_2 and NO_2^- decreased with the post-discharge time for the solutions with lower pH values [2]. In another application-oriented study, effects of plasma activated water has been investigated on the plant growth rate, in which thermal and non-thermal discharges in contact with or into the water led to the formation of H_2O_2, NO_2^- and NO_3^- species, accompanied by a decrease of the pH values [3].

In addition, the spectroscopic methods for estimating gas temperatures (T_{gas}) using the rotational temperatures of OH (A–X) or N_2 (C–B) bands are still one of the hot topics for the case of discharges with higher water vapor concentrations. The experimental study in [12] have shown the identical values of T_{rot} from both the OH (A–X) and N_2 (C–B) bands in the positive column of the atmospheric air discharges using a pin-to-water electrode configuration. While the measured values of T_{rot} from the OH (A–X) band are higher than those from the N_2 (C–B) band in the near cathode region, which proposes a question on how to accurately estimate the gas temperatures based on the spectroscopic methods. The similar situations also occur for the measurements of the gas temperatures in the region near the cathode for the atmospheric air discharges generated between a metallic anode and a flowing electrolyte solution cathode and in a saturated water vapor environment [13]. While in some other studies as of [25, 26], the values of T_{rot} from the N_2 (C–B) band were used to estimate the gas temperatures for the atmospheric air discharges in contact with liquids.

Therefore, the goal of this study is to investigate the characteristics of the AC-excited helium discharges in contact with liquid electrode as illustrated in section 2 under different operating conditions. The experimental studies include the current–voltage characteristics, the discharge emission patterns, and the spatial distributions of emission intensities and rotational temperatures just after initiation of the discharges in section 3, and temporal behaviors of the electrical and liquid characteristics, discharge emission patterns and the secondary species concentrations with the discharge time in section 4, accompanied by the conclusions in section 5.

2. Experimental setup

The experimental setup and the relative position of the discharge cell to the surface of the de-ionized (DI) water are illustrated in figures 1(a) and (b), respectively. For the discharge cell, a metallic syringe needle electrode is located coaxially in a conical quartz tube, where the position of the needle tip is fixed at 12.0 mm away from the outlet of the conical quartz tube. The electrode gap spacing (L_{gap}) is defined as the distance between the needle tip and DI water surface, while the relative distance between the conical tube exit and the DI water surface is denoted as L_+; thus, we have the relationship L_{gap} (mm) $= L_+ + 12.0$ (mm). The discharge cell is mounted in a chamber having a volume of 960 cm^3 which is filled up to 400 ml with the fresh DI water ($\sigma_0 = 20\ \mu S\ cm^{-1}$) before experiments. An external cooling system is connected to the chamber to keep the water temperature below 25 °C during experiments. The needle electrode is connected to an AC power supply with a driving frequency of $f = 22$ kHz (CTP-2000K, Nanjing Suman Electronics Corp.), while the DI water works as a grounded electrode. Helium with a high purity of 99.99% is used as the plasma forming gas, and is issued into the discharge region through the hollow needle electrode. The helium flow rate is fixed at $Q = 0.4$ slpm for all the experiments in this study. The electrical characteristics of the discharges are measured by a high voltage probe (Tektronix P6015A) and a current probe (Tektronix TCP0030A) through a digital oscilloscope (Tektronix DPO4034). The optical emission of the discharges is collected by using an optical fiber connected to a spectrometer (Avantes, Avaspec Multi-Channel Spectrometer) with 2400 grooves mm^{-1} gratings having a 0.04–0.07 nm resolution. The spectrometer integration time is fixed at 1000 ms for the

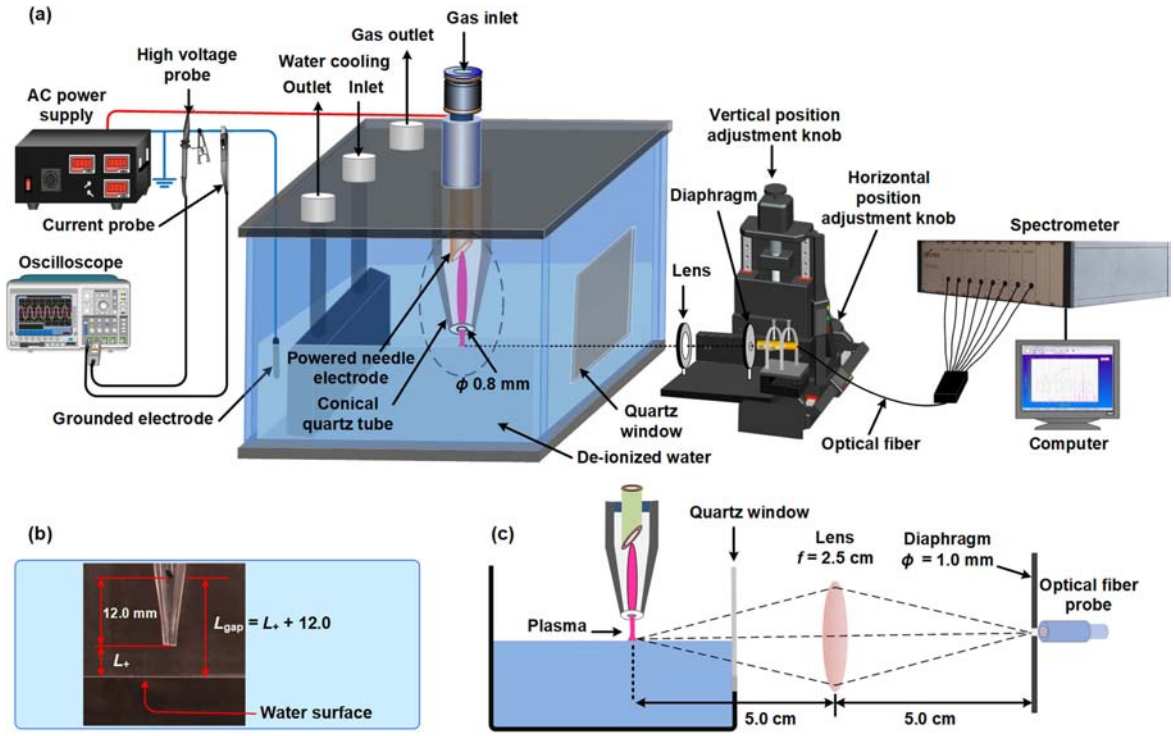

Figure 1. Experimental setup (a) and the discharge unit position relative to the liquid surface (b), and the illustration of the optical path used for the spatial measurements of the optical emission intensities from plasmas (c).

measurements in this study. To acquire the spatially resolved optical emission spectra of the discharges, a convex lens and a filed diaphragm are placed between the plasma reactor and the optical fiber which is located on a two-dimensional translational precision stage (GCD-202100M and GCD-203100 M, China Daheng Group, Inc.) with a positioning precision of 0.01 mm. As shown in figure 1(c), the spatial resolution of this optical emission spectroscopy system is 1.0 mm.

The concentrations of the secondary species (e.g., H_2O_2, NO_2^-, and NO_3^-) in the liquid phase are determined by using the spectrophotometric methods [27, 28]. The details are as follows: (i) the H_2O_2 concentrations are obtained based on the chemical reaction of H_2O_2 with Ti^{4+}, which results in an orange complex and obeys the Beer's law. In this technique, 1.6 ml of 2.0 mol l^{-1} sulfate acid and 1.6 ml of titanium potassium oxalate solutions are added sequentially into a Colorimetric tube which contains 2.0 ml liquid sample; then, the DI water is added until the total volume of the solution reaches 10.0 ml; and then, after 10 min, the absorbance of the solution is obtained using the spectrophotometer at 400 nm; and finally, the concentration of H_2O_2 is obtained based on the calibration curve. (ii) By mixing 3.0 ml treated sample with 1.0 ml color reagent (100.0 ml 85% phosphoric acid, 10.0 g Sulfanilamide and 1.0 g N-(1-naphthyl)-ethylenediamine dihydrochloride in 1.0 l water) in a Colorimetric tube first; then, adding the DI water until the total volume of the solution reaches 50.0 ml; and then, the solution absorbance is measured after 20 min using a spectrophotometer at a wavelength of 540 nm; and finally, the NO_2^- concentration is calculated through the calibration curve which obeys the Beer's law. (iii) In order to measure the concentrations of NO_3^-, 1.0 ml of 1.0 mol l^{-1} HCL and 0.1 ml of 0.8% sulfamic acid solutions are mixed consecutively into 3.0 ml of water sample in a Colorimetric tube, and keep the total volume of the solution be 25.0 ml by adding DI water; and then, the absorbance of the solution is taken through the ultraviolet spectrophotometer after 10 min. Since the dissolved organics show maximum at 220 and 275 nm, while NO_3^- only absorbs at 220 nm, thus, in order to get rid of the interference from the other dissolved organics, the reading at 275 nm is subtracted two times from the reading at 220 nm [28]; and finally, the NO_3^- concentration can be obtained through the calibration curve, which also obeys the Beer's law.

3. Characteristics of the discharges just after discharge initiation

3.1. Current–voltage characteristics and the discharge emission patterns

The current–voltage characteristics with an initial electrical conductivity of the DI water $\sigma_0 = 20\,\mu S\,cm^{-1}$, under different electrode gap spacings (L_{gap}) are shown in figure 2, where V_d and I_d represent the peak values of the discharge voltage and current, respectively. It is seen that: (i) the discharge first appears near the needle tip at $V_d = 1260$ V and $I_d = 3$ mA at a fixed gap spacing $L_{gap} = 17.0$ mm as shown in figure 2(a). With increasing in the discharge current, it expands gradually to occupy more space between the needle tip and the liquid surface. At this stage, it is diffuse and seems glow-like with a very weak optical emission as shown in

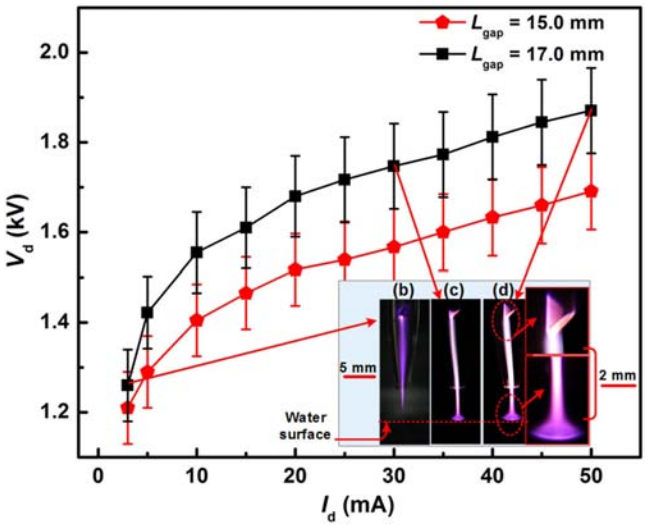

Figure 2. Peak values of V_d and I_d with the typical discharge images recorded under the exposure time of $t_{Exp} = 40$ ms.

figure 2(b). The discharge occupies entire gap spacing at $V_d = 1422$ V and $I_d = 5$ mA. With continuous increase of the discharge current from 5 to 50 mA, it appears like a constricted channel with an obvious increase of the emission intensity, especially in the region near the needle tip as illustrated in figures 2(c) and (d). This results from the stronger electric field in the vicinity of the needle tip at a higher discharge current [29]. (ii) Correspondingly, the diameters of the cone-shaped discharge structure near the gas–liquid interface also increase with increasing in the discharge current. (iii) At a fixed electrode gap spacing (e.g., $L_{gap} = 17.0$ mm), the discharge voltage increases with the discharge current. While under the same discharge current, the discharge voltage increases with the lengthening of the electrode gap spacing. In addition, the purple color of the discharges near the gas–liquid interface indicates the existence of N_2 diffusion into the discharge region from the ambient air since the discharge operates in an open atmosphere.

The current–voltage waveforms corresponding to the cases in figures 2(b)–(d) are presented in figures 3(a)–(c), respectively. It is seen that: (i) the current waveform corresponding to the case of figure 2(b) contains weak multiple current peaks (figure 3(a)), and the discharge appearance is glow-like. This discharge behavior is observed in experiments under the discharge current ranging from $I_d = 3$–5 mA. (ii) With an increase of the discharge current until 40 mA, a current pulsation appears at the beginning of the waveform positive half cycle (figure 3(b)). This indicates that the discharge turns into a streamer-like discharge mode (figure 2(c)). The similar characteristics were also observed for an AC-excited air–water discharges in helium environment [30]. (iii) Further increase of the discharge current results in shortening of the current pulsation duration and decreasing of the pulsation amplitude, and even completely disappears at a higher discharge current of 42 mA (figure 3(c)). This indicates that the ionization degree of the discharges increases with the increase of the discharge current.

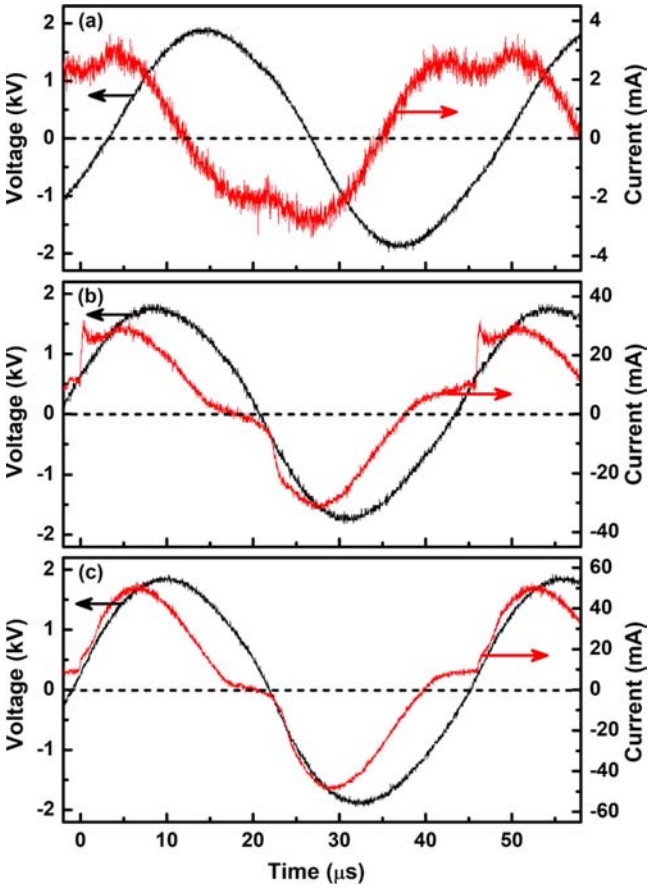

Figure 3. Current–voltage waveforms corresponding to the cases in figures 2(b)–(d).

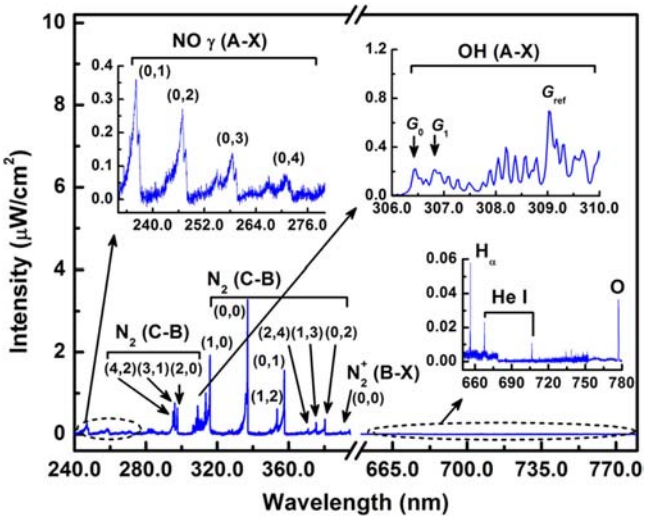

Figure 4. Overview of the typical emission spectrum recorded just after initiation of the discharge with $P_{in} = 26$ W.

3.2. Optical emission spectrum near the gas–liquid interface

Figure 4 shows the optical emission spectrum from the cone-shaped discharge structure at the gas–liquid interface (the optical fiber is located just above and parallel to the water surface) with the power input $P_{in} = 26$ W, $V_d = 1840$ V, $I_d = 38$ mA, $L_{gap} = 17.0$ mm and $\sigma_0 = 20$ μS cm^{-1}. It shows

that there exist various excited plasma species over a wide wavelength range 230–800 nm. The primarily dominated species include the N_2 (C–B) and NO γ (A–X) bands transition in the range of 230–385 nm; while the OH (A–X) band in the range of 306–310 nm, atomic He lines at 667.8 and 706.5 nm, hydrogen Balmer H_α and atomic O lines at 656.2 and 777.2 nm can also be observed from the spectrum. In addition, the nitrogen first negative system N_2^+ (B–X) is also observed in the range of 388–392 nm. The atomic oxygen (O) is a highly active agent in destroying cells, chemical or biological contaminations. The OH species with the high oxidation potential of 2.85 V are also important in the advanced oxidation processes for the removal of organic substances from the waste water. It is also the primary species for the formation of H_2O_2 which is another important species to remove the organic contamination from the waste water. In addition, the existence of NO in the gas phase region set the basis for the formation of NO_2^- and NO_3^- in the liquid phase, which are useful in the fields of biomedicine and agriculture.

The formation of the preceding chemically reactive species can be described by the chemical reaction pathways, (R1)–(R11). The diffusion of N_2 into the discharge region from the surrounding air favors the production of NO γ (A–X) by suppressing OH and O species (reactions (R1)–(R3)) [31], while nitrogen second positive system N_2 (C–B) in the emission spectrum comes from the pooling reaction between the N_2 metastable states, and with the electron impact excitation of N_2 ((R4) and (R5)) [32, 33]. The He metastables (He_{meta}) are responsible for the generation of nitrogen first negative system N_2^+(B–X) through the Penning ionization (R6) [34, 35]. The OH (A–X) band can be produced from the dissociative electron recombination of H_2O^+ (or H_3O^+), and with the dissociative electron recombination which leads to production of OH (X), and then, to excitation to OH (A) through the electron impact reaction ((R7)–(R9)) [36]. In addition, the He_{meta} collisions with H_2O molecules can also lead to the formation of OH (A–X) via direct dissociative excitation due to the higher potential energy (19.8 eV) of He_{meta} (R10) [37]. The occurrence of the atomic O line in the emission spectrum is due to the electron impact dissociation (R11) [38].

$$N_2(A^3\Sigma_u^+) + O \rightarrow N + NO \quad (R1)$$

$$OH + N \rightarrow H + NO \quad (R2)$$

$$N + O + M \rightarrow M + NO \quad (R3)$$

$$N_2(A^3\Sigma_u^+) + N_2(A^3\Sigma_u^+) \rightarrow N_2(X^1\Sigma_g^+) + N_2(C^3\Pi_u) \quad (R4)$$

$$N_2\left(X^1\Sigma_g^+\right) + e \rightarrow N_2(C^3\Pi_u) + e \quad (R5)$$

$$N_2 + He(2^3S) \rightarrow He + N_2^+(B^2\Sigma_u^+) + e \quad (R6)$$

$$H_2O^+(H_3O^+) + e \rightarrow OH(A) + \ldots \quad (R7)$$

$$H_2O^+(H_3O^+) + e \rightarrow OH(X) + \ldots \quad (R8)$$

$$OH(X) + e \rightarrow OH(A) + e \quad (R9)$$

$$He_{meta} + H_2O \rightarrow H^+ + OH(A) + He + e \quad (R10)$$

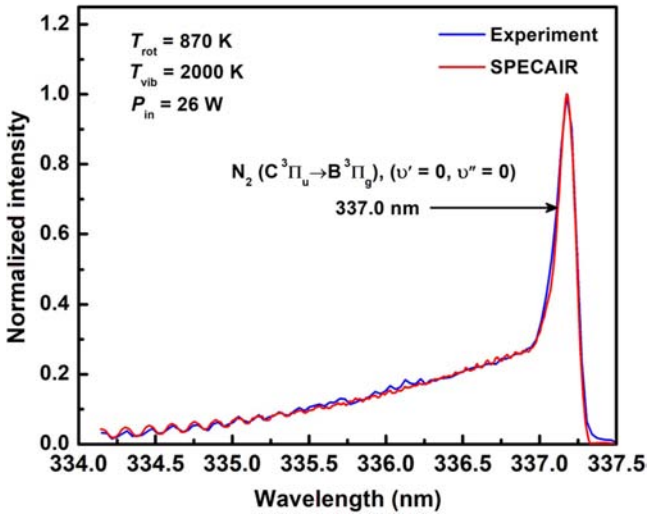

Figure 5. SPECAIR fit to the experimental spectrum for the determination of the T_{rot} and T_{vib}.

$$H_2O + e \rightarrow O(3p^5P) + H_2 + e. \quad (R11)$$

3.3. Spatial distributions of emission intensities and temperatures

In this study, the rotational (T_{rot}) and vibrational (T_{vib}) temperatures are derived from the measured optical emission spectrum of the discharges. There are two methods for the determination of the rotational temperatures (T_{rot}). The first method is based on the OH (A–X) band, which employs the relative intensity of the unresolved band heads G_0, G_1, and G_{ref} at 306.5 nm, 306.8 nm, and 309.0 nm [39], respectively, as shown in the inset of figure 4. In the present study, the ratios G_0/G_{ref} are used for estimation of the T_{rot} from the tables provided in [39], which was validated by the interferometric measurements elsewhere [40]. The second method employs the N_2 (C–B) band by fitting the experimental spectrum for (0, 0) transition located at 337.0 nm with the synthetic spectrum generated by using the simulations with the SPECAIR code [41]. In addition, the SPECAIR code also provides the value of T_{vib} [42]. The estimated rotational temperature from the (0, 0) transition at 337.0 nm agrees with the experimental accuracy of the N_2 (C–B) band for (0, 2) transition at 380.4 nm [9]. A SPECAIR fit to a typical spectrum recorded for the discharge region near the gas–liquid interface with $P_{in} = 26$ W is presented in figure 5 with the derived rotational and vibrational temperatures of 870 K and 2000 K, respectively.

The spatially resolved profiles of the emission intensities of OH (A–X) band at 309.0 nm, N_2 (C–B) band at 337.0 nm, NO γ (A–X) band at 236.0 nm and atomic O line at 777.2 nm along the geometrical axis of the discharge cell just after initiation of the discharge under the same operating conditions as those in figure 4 are shown in figure 6(a). It shows that the optical emissions of N_2 (C–B) and NO γ (A–X) bands corresponding to the discharge region are low and constant

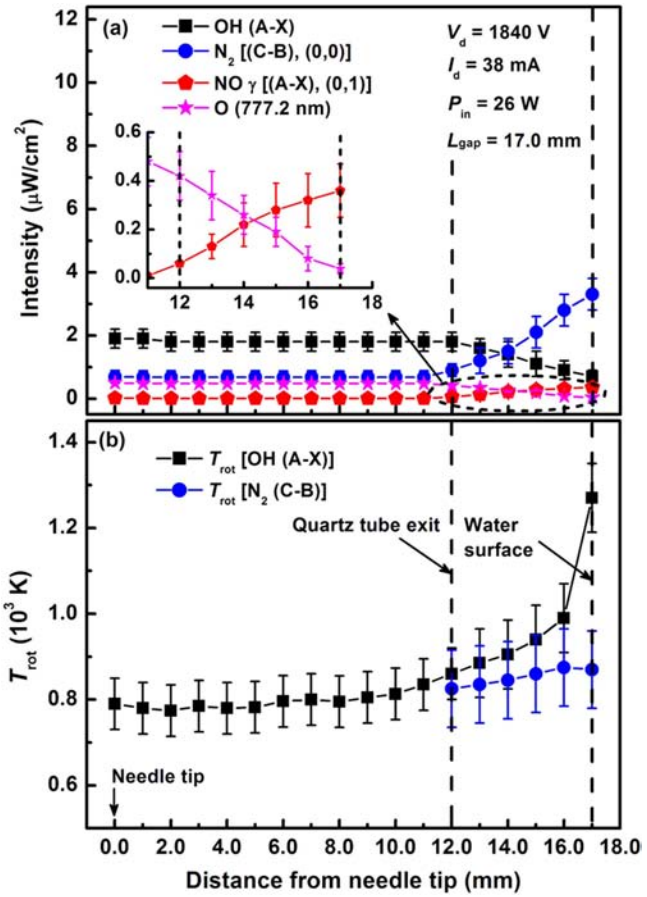

Figure 6. The emission intensity distributions of OH (A–X), N_2 (C–B), NO γ (A–X) bands and atomic O line (a), and the estimated T_{rot} of OH (A–X) and N_2 (C–B) bands (b), just after initiation of the discharges with $P_{in} = 26$ W.

since the discharges are enclosed inside the conical tube with no air entrainment. At the outside of the conical quartz tube, the emission intensities of the N_2 (C–B) and NO γ (A–X) bands increase, while at the same time, those of OH (A–X) and O decrease obviously. This phenomenon results from the engulfment of the surrounding air between the conical quartz tube exit and the water surface, which favors the formation of NO γ (A–X) by suppressing OH and O species ((R1)–(R3)) as discussed in section 3.2 [31]. Near the gas–liquid interface, the maximum emission intensities of NO γ (A–X) and N_2 (C–B), and simultaneously the minimum intensities from OH (A–X) and O, indicate that there exists very active discharge chemistry in this region, which suits well for the formation of NO_2^- and NO_3^- species.

Figure 6(b) shows the spatial distributions of the derived rotational temperatures of OH (A–X) and N_2 (C–B) bands corresponding to the emission intensity distributions in figure 6(a). As mentioned above, since the intensity of N_2 (C–B) band inside the conical tube is very small, a precise measurement of the T_{rot} from the N_2 (C–B) band are not possible. So, just the values of the T_{rot} from OH (A–X) band inside the conical tube are provided here. It is seen from figure 6(b) that: (i) at the conical tube exit, the values of T_{rot} from both the OH (A–X) and N_2 (C–B) bands are close to each other. (ii) With approaching the water surface, the T_{rot} of OH (A–X) increases from 885 to 1270 K, especially with a significant increase in the vicinity of the gas–liquid interface; while the variation of T_{rot} of N_2 (C–B) band is very small. In our opinion, the higher water vapor concentration in the vicinity of the gas–liquid interface will boost up the OH quenching, which leads to an inefficient rotational energy transfer, and thus, prevents the thermalization of the rotational population distribution resulting in the higher values of T_{rot} from the OH (A–X) band than that from the N_2 (C–B) band [24]. Therefore, the selection of N_2 (C–B) band, to our opinion, should be a better choice for the determination of T_{gas} in this study.

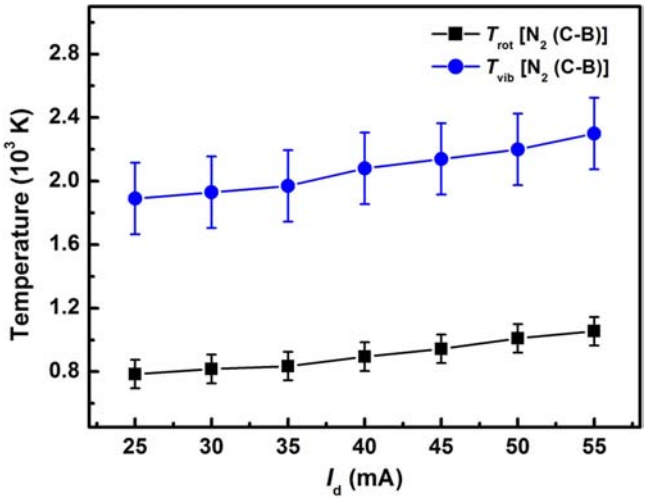

Figure 7. Variations of the T_{rot} and T_{vib} as a function of the discharge current just after initiation of the discharges with $P_{in} = 26$ W.

Variations of the rotational and vibrational temperatures from the N_2 (C–B) band at the gas–liquid interface with increasing in the discharge current are shown in figure 7. It shows that both the rotational and vibrational temperatures increase from 785 K to 1055 K and from 1890 K to 2300 K, respectively. This growing tendency of the temperatures with the increase of the discharge current indicates that the physical–chemical processes become stronger under the higher discharge current magnitudes at the gas–liquid interface.

4. Temporal behaviors of the discharges

The temporal evolutions of the discharge voltage (V_d) and current (I_d) with the discharge time (t_d) for the case of $P_{in} = 26$ W, $V_d = 1840$ V, $I_d = 38$ mA, $L_{gap} = 17.0$ mm and $\sigma_0 = 20\ \mu S\ cm^{-1}$ are shown in figure 8(a). It is shown that starting from the initiation of the discharge, the discharge voltage decreases from 1840 to 1350 V, while the value of I_d increases from 38 to 51 mA during the 120 min discharge process. At the same time, the considerable changes in the pH values and the liquid electrical conductivities (σ) also occur, as shown in figure 8(b). During the discharges, the pH values of the liquid decrease from 7.5 to 3.2 accompanied by an increase of the electrical conductivities from 20 to

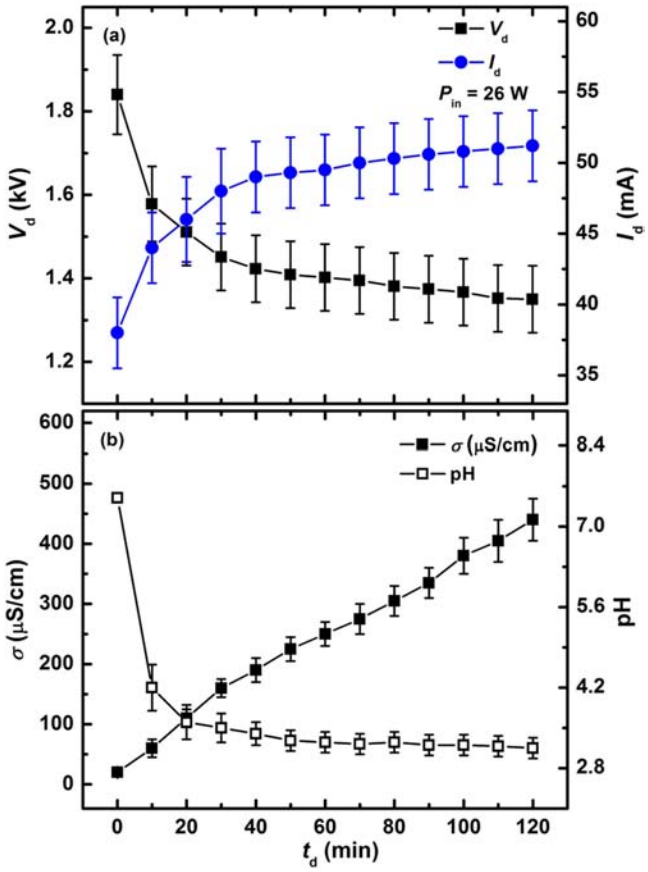

Figure 8. Variations of the peak values of V_d and I_d (a), and the corresponding variations of the pH values and the liquid electrical conductivities (b) as a function of t_d with constant power input $P_{in} = 26$ W.

440 μS cm^{-1}. Accompanied with the variations of the electrical features and the properties of the liquid, the emission patterns of the discharges also show an obvious change with the discharge time. As shown in figure 9, with the extending of the discharge time (t_d), the diameter of the cone-shaped discharge structure at the gas–liquid interface decreases. The changes in the pH value and σ indicate the variations of the liquid properties with the formation of the new species in the liquid phase, e.g., H_2O_2, NO_2^-, and NO_3^-. The variations of the electrical conductivities are the result of HNO_3 formation, since the NO species produced in the gas phase lead to the formation of the acidic products in the liquid phase via the reactions (R12)–(R15) [2, 22, 31], which will be discussed later. And the variation of the electrical conductivity also gives an explanation to the increase of the discharge current since the initiation of the discharges. In this section, the concentrations of H_2O_2, NO_2^- and NO_3^- are obtained by using the Colorimetric methods [27, 28] as described in detail in section 2. A spectrophotometer is used to determine the solution absorbance, and the final concentrations are obtained from the calibration curves, which follow the Beer's law. It should be emphasized that the treated samples are immediately analyzed after collecting from the solution chamber.

To understand the formation chemistry of the secondary species, a schematic of the chemical reaction processes in both the gas and liquid phases is presented in figure 10. It shows that, outside the conical tube, the surrounding air boosts up the chemical processes in the plasma region; as a consequence, the reactive nitrogen species such as NO increases. This has been proved by the spatial profiles of the optical emissions from plasmas in section 3.3. As shown in figure 10, the generated NO species are either converted into NO_2 via reacting with N_2 and O in the gas phase discharges or penetrate directly into the liquid and induce further chemical reactions; while the generated NO_2 are converted into NO_2^- and NO_3^- either at the gas–liquid interface or into the liquid via reacting with H_2O molecules. Formation of the NO_2^- and NO_3^- species would result in liquid acidification. In addition, the liquid phase recombination of OH radicals coming from gas phase ((R7)–(R10)) [36, 37] results in the production of H_2O_2. And thus, the disproportionation of NO_2^- into NO_3^- species via H_2O_2, H^+ and H_2O occurs as shown in figure 10.

Figure 11 shows the instantaneous concentrations of H_2O_2, NO_2^- and NO_3^- with the discharge time (t_d) for the case of $P_{in} = 26$ W. The chemical reactions induced into liquid by plasmas in the gas–liquid environment are as follows:

$$N_2 + O + NO \rightarrow N_2 + NO_2 \quad \text{(R12)}$$

$$NO_2 + OH \rightarrow HNO_3 \quad \text{(R13)}$$

$$HNO_3(aq) \rightarrow H^+ + NO_3^- \quad \text{(R14)}$$

$$H_2O + 2NO_2(aq) \rightarrow 2H^+ + NO_2^- + NO_3^- \quad \text{(R15)}$$

$$OH + OH \rightarrow H_2O_2 \quad \text{(R16)}$$

$$H_2O_2 + NO_2^- + H^+ \rightarrow H_2O + NO_3^- + H^+ \quad \text{(R17)}$$

$$3NO_2^- + H^+ + H_2O \rightarrow NO_3^- + 2NO + H_3O^+. \quad \text{(R18)}$$

The reactions (R12)–(R15) [2, 22, 31] show the formation processes of NO_2^- and NO_3^- via NO species. While reaction (R16) represents the production of H_2O_2 species via OH recombination process [43]. It is seen from figure 11 that the instantaneous concentrations of the secondary species vary considerably with t_d. At the early stage of the discharges, the concentrations of NO_2^- and NO_3^- increase monotonically with t_d through the chemical reactions (R12)–(R15), accompanied by the decrease of the liquid pH values (acidification) and the increase of the solution electrical conductivities (figure 8(b)); while at later stage of the discharges, the concentrations of H_2O_2 and NO_2^- decreases with the formation of NO_3^- via (R17). In addition, with the solution acidification, the chemical reaction, (R18), results in the disproportionation of NO_2^- into NO_3^- with t_d [44]. Therefore, on one hand, the liquid acidification with t_d is helpful for the formation of NO_3^-, while on the other hand, it reduces the concentrations of H_2O_2 and NO_2^-, since the chemical reactions (R17) and (R18) can only be stimulated in the acidic environment. Apart from these, the decreasing concentrations of H_2O_2 and NO_2^- with t_d can also be explained based on the optical emission patterns, in which the diameter of the cone-shaped discharge structure at the gas–liquid interface decreases (figure 9). The shrink of the discharge channel results in the formation reduction of the primary species such as OH and NO, which further leads to

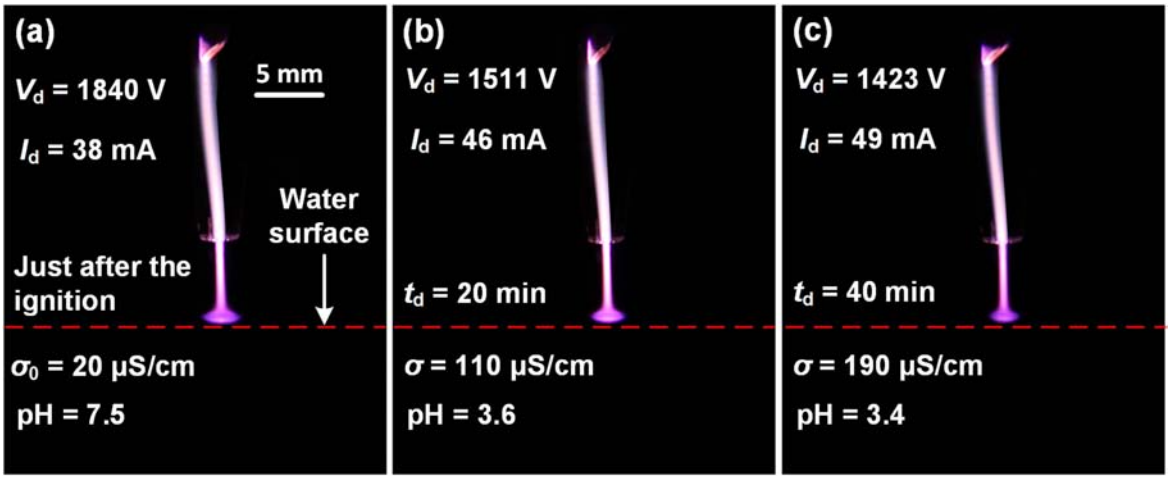

Figure 9. The discharge images as a function of t_d recorded under the exposure time of $t_{Exp} = 40$ ms and $P_{in} = 26$ W.

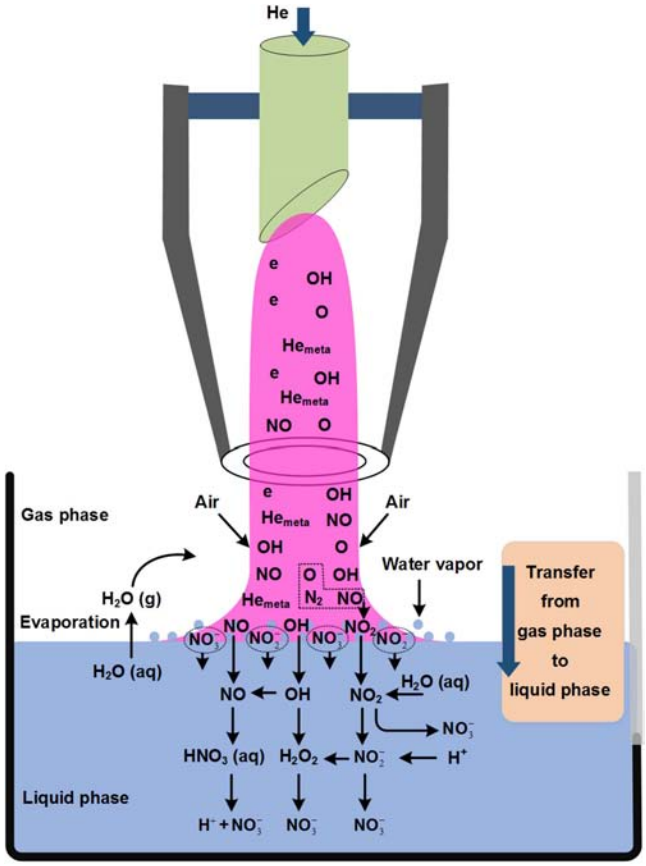

Figure 10. Schematic of the chemical reaction processes in the gas phase and into the liquid.

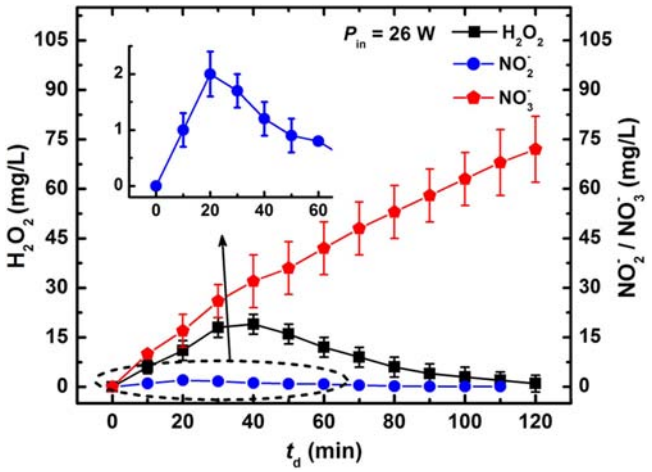

Figure 11. Variations of the instantaneous concentrations of H_2O_2, NO_2^- and NO_3^- species in the liquid phase as a function of t_d with constant power input $P_{in} = 26$ W.

the lowering of the production of H_2O_2 and NO_2^- via the reactions (R12), (R15) and (R16).

5. Concluding remarks

In this paper, the AC-excited helium discharges generated in contact with the DI water electrode are investigated. The major conclusions are as follows:

(1) The experimental results just after initiation of the discharges show that: (i) for the fixed gap spacing, increase of the discharge current results in the increase of the discharge voltage and the diameter of the cone-shaped discharge structure at the gas–liquid interface. (ii) In the vicinity of the gas–liquid interface, the presence of surrounding air and water vapor boosts up various physical–chemical processes. (iii) The reliable rotational temperature obtained from the N_2 (C–B) band at the gas–liquid interface is 870 K with the power input of 26 W.

(2) The experimental results also show a significant temporal behavior of the helium discharges with the discharge time. The increase of the instantaneous concentrations of NO_2^- and NO_3^- in liquid with the discharge time leads to a drop of the liquid pH values (acidification) and the increase of the electrical conductivities of the solutions.

Although these experimental results are helpful for understanding the physical characteristics of the discharges in

contact with liquids, especially for understanding the formation mechanisms of various primary and secondary species during discharges, the influences of the surrounding air, which may diffuse into the gas-phase discharge region or dissolve into liquid, on the discharge mechanisms and characteristics of plasmas need to be investigated systematically in future research. This would be vital for promoting potential applications of such type of discharges in the fields of environment, biomedicine, agriculture, etc.

Acknowledgments

This work has been supported by the Major Science and Technology Program for Water Pollution Control and Treatment (No. 2014ZX07215-001) and partly by National Natural Science Foundation of China (Nos. 11475103, 51578309). In addition, Mr Qazi highly acknowledges the Chinese Scholarship Council for the financial assistance of my PhD program in Tsinghua University of China.

References

[1] Tatarova E *et al* 2014 *Plasma Sources Sci. Technol.* **23** 063002
[2] Lukes P *et al* 2014 *Plasma Sources Sci. Technol.* **23** 015019
[3] Park D P *et al* 2013 *Curr. Appl. Phys.* **13** S19
[4] Mariotti D *et al* 2012 *Plasma Process. Polym.* **9** 1074
[5] Bruggeman P J *et al* 2016 *Plasma Sources Sci. Technol.* **25** 053002
[6] Liu D X *et al* 2010 *Plasma Sources Sci. Technol.* **19** 025018
[7] Liu D X *et al* 2016 *Sci. Rep.* **6** 23737
[8] Zheng P *et al* 2015 *Plasma Sources Sci. Technol.* **24** 015010
[9] Bruggeman P *et al* 2008 *Plasma Sources Sci. Technol.* **17** 025012
[10] Chen Q *et al* 2008 *Thin Solid Films* **516** 6688
[11] Ognier S *et al* 2009 *Plasma Chem. Plasma Process.* **29** 261
[12] Bruggeman P *et al* 2008 *J. Phys. D: Appl. Phys.* **41** 215201
[13] Mezei P, Cserfalvi T and Csillag L 2005 *J. Phys. D: Appl. Phys.* **38** 2804
[14] Qazi H I A *et al* 2015 *Phys. Plasmas* **22** 123512
[15] Wang J *et al* 2016 *Plasma Sci. Technol.* **18** 370
[16] Lukes P and Locke B R 2005 *J. Phys. D: Appl. Phys.* **38** 4074
[17] Locke B R and Shih K-Y 2011 *Plasma Sources Sci. Technol.* **20** 034006
[18] van Gessel A F H, Alards K M J and Bruggeman P J 2013 *J. Phys. D: Appl. Phys.* **46** 265202
[19] Kong M G *et al* 2009 *New J. Phys.* **11** 115012
[20] Chen Z *et al* 2016 *Plasma Process. Polym.* **13** 1151
[21] Cheng H *et al* 2016 *High Volt.* **1** 62
[22] Takaki K *et al* 2013 *J. Phys.: Conf. Ser.* **418** 012140
[23] Šunka P 2001 *Phys. Plasmas* **8** 2587
[24] Bruggeman P *et al* 2009 *Plasma Process. Polym.* **6** 751
[25] Titov V A *et al* 2006 *Plasma Chem. Plasma Process.* **26** 543
[26] Lu X P and Laroussi M 2005 *IEEE Trans. Plasma Sci.* **33** 272
[27] Sellers R M 1980 *Analyst* **105** 950
[28] Rice E W *et al* 2012 *Standard Methods for the Examination of Water and Wastewater* 22nd edn (Washington DC: American Public Health Association (APHA), American Water Works Association (AWWA) & Water Environment Federation (WEF))
[29] Sun B, Sato M and Clements J S 1997 *J. Electrostat.* **39** 189
[30] Park J Y *et al* 2006 *J. Phys. D: Appl. Phys.* **39** 3805
[31] Eichwald O *et al* 1997 *J. Appl. Phys.* **82** 4781
[32] Bibinov N K, Fateev A A and Wiesemann K 2001 *J. Phys. D: Appl. Phys.* **34** 1819
[33] Tsuji M *et al* 2003 *Appl. Surf. Sci.* **217** 134
[34] Liu D X *et al* 2016 *High Volt.* **1** 81
[35] Sublet A *et al* 2006 *Plasma Sources Sci. Technol.* **15** 627
[36] Verreycken T *et al* 2010 *Plasma Sources Sci. Technol.* **19** 045004
[37] Yamada H *et al* 2016 *J. Phys. D: Appl. Phys.* **49** 394001
[38] Rehman F, Lozano-Parada J H and Zimmerman W B 2012 *Int. J. Hydrog. Energy* **37** 17678
[39] de Izarra C 2000 *J. Phys. D: Appl. Phys.* **33** 1697
[40] Rabat H and de Izarra C 2004 *J. Phys. D: Appl. Phys.* **37** 2371
[41] Laux C O 2002 www.specair-radiation.net
[42] Laux C O *et al* 2003 *Plasma Sources Sci. Technol.* **12** 125
[43] Chen B *et al* 2016 *Plasma Sci. Technol.* **18** 41
[44] Machala Z *et al* 2013 *Plasma Process. Polym.* **10** 649